

Influenza virus binds its host cell using multiple dynamic interactions

Christian Sieben^{a,1}, Christian Kappel^{b,1}, Rong Zhu^c, Anna Wozniak^d, Christian Rankl^e, Peter Hinterdorfer^c, Helmut Grubmüller^{b,2}, and Andreas Herrmann^{a,2}

^aDepartment of Biology, Molecular Biophysics, Humboldt University Berlin, 10115 Berlin, Germany; ^bDepartment of Theoretical and Computational Biophysics, Max Planck Institute for Biophysical Chemistry, 37077 Göttingen, Germany; ^cInstitute for Biophysics, Johannes Kepler Universität Linz, 4040 Linz, Austria; ^dJPK Instruments Aktiengesellschaft, 12435 Berlin, Germany; and ^eAgilent Technologies, 4020 Linz, Austria

Edited by Peter Palese, Mount Sinai School of Medicine, New York, NY, and approved July 20, 2012 (received for review December 8, 2011)

Influenza virus belongs to a wide range of enveloped viruses. The major spike protein hemagglutinin binds sialic acid residues of glycoproteins and glycolipids with dissociation constants in the millimolar range [Sauter NK, et al. (1992) *Biochemistry* 31:9609–9621], indicating a multivalent binding mode. Here, we characterized the attachment of influenza virus to host cell receptors using three independent approaches. Optical tweezers and atomic force microscopy-based single-molecule force spectroscopy revealed very low interaction forces. Further, the observation of sequential unbinding events strongly suggests a multivalent binding mode between virus and cell membrane. Molecular dynamics simulations reveal a variety of unbinding pathways that indicate a highly dynamic interaction between HA and its receptor, allowing rationalization of influenza virus–cell binding quantitatively at the molecular level.

multivalency | adhesion | avidity | tropism

Influenza virus is a highly contagious pathogen that causes annual epidemics in the human population. The viral envelope contains two spike proteins, hemagglutinin and neuraminidase (NA), as well as the proton channel M2. HA, organized as a homotrimer (1), mediates the initial binding to the target membrane and the fusion of the viral envelope with the endosomal membrane. The crystal structure of the viral HA bound to its cellular receptor, sialic acid (SA), shows that the receptor-binding domain is located in the HA1 subunit (2). The minimal receptor of human influenza viruses is SA coupled to galactose via an α -2,6-glycosidic linkage. The glycan topology of the human respiratory tract was shown to be very complex, but 2,6-linked SA has an overall predominance on glycoproteins and glycolipids on the surface of ciliated cells of the human respiratory epithelium (3). However, HA interacts with at least three of the terminal sugars and thus, the pentasaccharide lactoseries tetrasaccharide c (LSTc) appears to be the receptor of human influenza virus *in vivo* (4).

Virus–host cell binding marks the first critical step of infection. Hence, forces involved in this process are essential. Optical tweezers (OT) and atomic force microscopy (AFM)-based single-molecule force spectroscopy (SMFS) provide powerful tools to measure these forces in biological systems (5, 6). However, an assignment of forces to their underlying molecular interactions involved in these processes is difficult or cannot even be obtained by these techniques. In molecular dynamics (MD), time-dependent interactions between all atoms within a given system are calculated numerically. Force-probe molecular dynamics simulations (FPMD) extend this method by introducing a moving harmonic potential as a “virtual spring” acting on given atoms (7).

We applied single-virus force spectroscopy (SVFS) to characterize the interacting forces between influenza A viruses (H3N2 and H1N1) and living cells. Our study reveals binding forces between HA and its receptor of approximately 10–25 pN. This and the observation of stepwise unbinding events strongly indicate a multivalent binding mode (i.e., multiple virus–cell interactions) to adhere the virus stably to the cell surface. Using FPMD we

found that the receptor-binding domain of HA is very rigid and does not show any deformations during unbinding of the ligand, which does not argue for any cooperativity between HA monomers in binding. The observed unbinding pathways are diverse and contain zipper-like as well as all-or-none unbinding events. This highly dynamic behavior of the interaction was also observed by SVFS and led to a broad distribution of measured unbinding forces. Notably, we did not find a clear preference for binding of the probed influenza strains to one of the cell lines differing in the structure of the SA receptors.

Results

Single-Virus Force Measurements Using Optical Tweezers. Proteins show fast and strong adsorption on polystyrene (PS) surfaces (8). We coated 1.5- μ m PS beads with influenza A X-31 virions (Fig. 1A). The coating was optimized to allow single virus–receptor force measurements (*SI Materials and Methods* and Figs. S1 and S2). One day prior to the experiment the cells were seeded at a density of $1\text{--}5 \cdot 10^5$ cells per petri dish. The virus-coated beads were added, trapped, and moved to a position 3–5 μ m from the cell border. The distance and the speed were set and each extend–retract cycle was repeated 1–5 times. We then changed the bead and the position on the cell. We chose clear and sharp edges of the cell to ensure that the bead was not in contact with filopodia or other cell extensions (Movie S1). The contact force was kept between 5 and 50 pN and the bead was retracted without delay to reduce the chance of multiple bindings (Fig. 2A). For CHO cells we found rupture forces of approximately 12 pN for a pulling velocity of 200 nm/s. Similarly, for Madin–Darby canine kidney (MDCK) cells we found a maximum frequency of approximately 10 pN at the same retraction speed. In contrast to CHO cells, for MDCK cells we found a significant amount of rupture events that happen at higher forces, with a maximum at approximately 23 pN, which corresponds to the virus bound to multiple receptors (Fig. S3). This observation might be a consequence of an approximately 30% higher amount of surface SA on MDCK cells (Fig. S4).

To verify that viruses bind specifically to SA, we assessed virus binding upon removal of terminal SA residues by NA treatment of cells (*SI Materials and Methods*). Cell surface SA was labeled by binding of *Sambucus nigra* lectin (SNA; specific for 2,6 linkages) and *Maackia amurensis* lectin (MAA; specific for 2,3 linkages) and quantified by flow cytometry (Fig. S4). In force measurements, we found that after NA treatment the rupture forces were

Author contributions: C.S., C.K., P.H., H.G., and A.H. designed research; C.S., C.K., R.Z., and A.W. performed research; C.R. contributed new reagents/analytic tools; C.S., C.K., and R.Z. analyzed data; and C.S., C.K., P.H., H.G., and A.H. wrote the paper.

The authors declare no conflict of interest.

This article is a PNAS Direct Submission.

¹C.S. and C.K. contributed equally to this work.

²To whom correspondence may be addressed. E-mail: andreas.herrmann@rz.hu-berlin.de or hgrubmu@gwdg.de.

This article contains supporting information online at www.pnas.org/lookup/suppl/doi:10.1073/pnas.1120265109/-DCSupplemental.

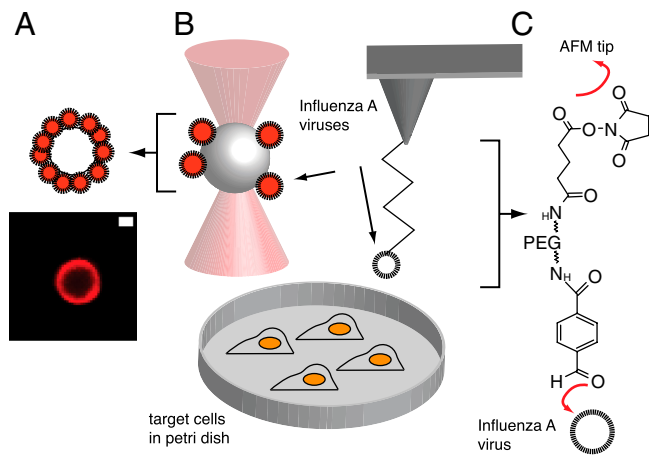


Fig. 1. Schematic of SVFS experiments using optical tweezers and atomic force spectroscopy. (A) R18-labeled influenza virions were adsorbed to polystyrene beads as verified by confocal microscopy. Scale bar, 0.5 μm . Using optical tweezers, binding forces were measured between viruses on beads and adherent cells grown in glass-bottom Petri dishes (B, Left). For AFM experiments, virions were covalently tethered to the AFM tip by a bifunctional PEG cross-linker (C). The functionalized cantilever was lowered on cells and forces were detected during retraction (B, Right).

similar compared to cells without NA treatment, although the binding probability was strongly reduced by 60–70% of the control. This indicates specific interactions between the viral HA and SA residues. However, to increase the chance for single rupture detection we used CHO cells for all further OT measurements.

Varying the pulling velocity (v) led to a dynamic force spectrum. The loading rate was calculated by multiplying the retraction velocity (v) with the effective spring constant, k_{eff} , where k_{eff} is the slope of the force distance curve at rupture. Plotting the loading rate versus the measured rupture force revealed a linear dependence (Fig. 2B). According to the theory, this dependence indicates that a single energy barrier is crossed in the thermally active regime (9). From the plot in Fig. 2B, the separation from the energy barrier, x_u , and the kinetic off-rate constant, k_{off} , can be determined by fitting the curve to Eq. S1 (SI Materials and Methods). The values for CHO cells were $x_u = 3.4 \pm 4.23 \text{ nm}$ and $k_{\text{off}} = 0.12 \pm 1.23 \text{ s}^{-1}$.

Single-Virus Force Measurements using AFM. Influenza virions from strains H3N2 and H1N1 were covalently attached to AFM cantilevers (10). We used CHO, MDCK, and A549 cells, and their surface SA composition was characterized by a lectin binding assay (SI Materials and Methods). Although MDCK and A549 cells

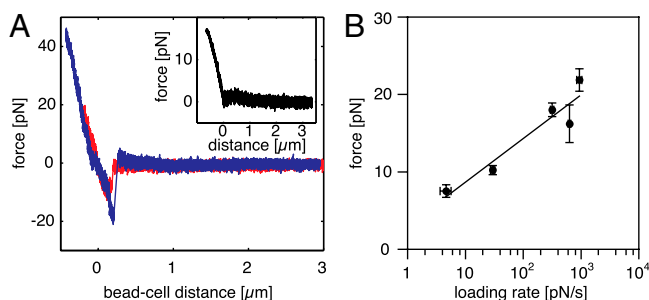


Fig. 2. SVFS measurements using optical tweezers. Virus-coated beads were moved toward a cell until touching, and subsequently retracted. Single rupture events of different height were recorded (A). When the bead surface was blocked with BSA, no interaction could be detected (A, Inset). Dynamic force spectrum of a single virus–receptor interaction on the surface of CHO cells (B). The error bars account for the uncertainties in the determination of the spring constant and in finding the most probable rupture force.

clearly express 2,6-linked SA, CHO cells only express 2,3-linked SA (Fig. S4). The cantilever was moved above a suitable cell and lowered until touching the plasma membrane. Force distance curves were recorded at various pulling velocities to allow dynamic force spectroscopy analysis of the underlying interaction. For both virus strains we found rupture forces between 10 and 25 pN. Interestingly, we did not find a clear preference for one of the studied cell lines. We observed single and stepwise unbinding events, which indicate the rupture of individual receptor molecules (Fig. 3A and B). Rarely, we observed rupture events at higher forces ($>30 \text{ pN}$), pointing at the simultaneous rupture of multiple bonds. Increase of the pulling velocity led to an increase of the most probable rupture force with a linear loading rate dependence (Fig. 3C and D). Fitting the force spectra to Eq. S1 revealed the kinetic off-rate constant and the separation of the bound state to the energy barrier (Table 1).

Molecular Dynamics Simulation of the HA–Receptor Interaction. To investigate the structural and energetic determinants of the HA–receptor unbinding process, we employed force-probe MD simulations. As a starting structure we used the full HA trimer of influenza A X-31 bound to the cell surface receptors LSTa and LSTc (4) (Fig. S5, Lower). In the simulations using nine different loading rates, the receptors were removed from the HA trimer in parallel, as well as individually, from each of the three monomers (Movie S2). Interestingly, the behavior and the mean peak forces of LSTa and LSTc are very similar (Fig. S7). In the following section we will discuss the MD simulation results of LSTc in more detail. Two orientations of the receptor with respect to the pulling direction were present. The receptor was either aligned parallel (receptors B and C in Fig. S5) or orthogonal to the pulling direction (receptor A in Fig. S5). In addition, because of thermal fluctuations in the equilibrium simulation that preceded the unbinding simulations, the three receptors owned slightly different conformations and, accordingly, slightly different interactions to HA. These conformations can therefore be considered independent for each chosen starting structure. In all receptor conforma-

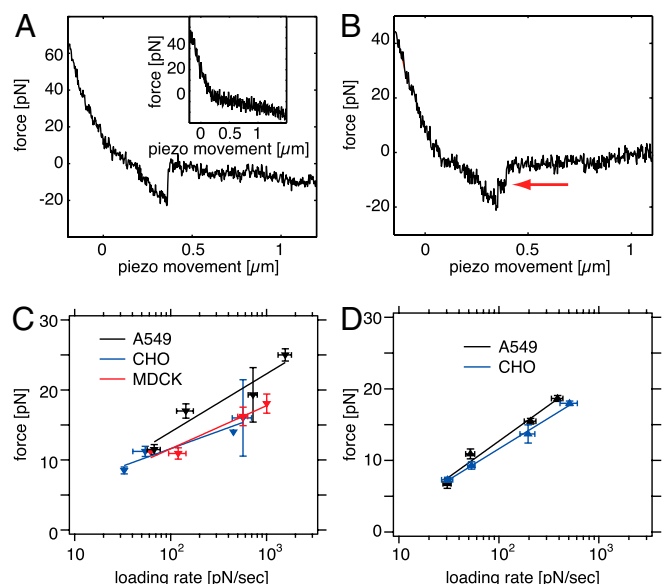


Fig. 3. SVFS measured by AFM in force spectroscopy mode. Virus interacting with a single receptor (A) and with multiple receptors (B), which produced serial rupture events (B, arrow). When the cantilever was blocked with BSA, no interaction could be detected (A, Inset). Variation of the pulling velocity led to an increase of the measured most-probable unbinding force. Dynamic force spectra of influenza A virus X-31 (C) and A/WSN/32 (D) interacting with single receptors on living cells. Error bars account for the uncertainties in the determination of the spring constant and in finding the most probable rupture force.

Table 1. Separation from the energy barrier x_u , kinetic off rate k_{off} , and average bond lifetime τ_{off} obtained from fits of data in Fig. 3 C and D to Eq. S1

	k_{off} (s^{-1})	x_u (nm)	τ_{off} (s)
H3N2 A549	0.64 ± 0.52	0.42 ± 0.41	1.6
H3N2 CHO	0.18 ± 0.17	2.61 ± 3.11	5.5
H3N2 MDCK	0.45 ± 0.35	0.84 ± 0.79	2.2
H1N1 A549	1.22 ± 0.32	0.18 ± 0.06	0.8
H1N1 CHO	1.16 ± 0.13	0.24 ± 0.03	0.9

tions, hydrogen bonds formed between each receptor and four residues from the HA head groups: Tyr98, Gly135, Ser136, and Asn137. Depending on each conformation, additional hydrogen bonds involving other residues were present (Table S1). During the unbinding simulations we observed force profiles with single peaks (receptor B) as well as multiple peaks (receptor A and C) (Fig. 4, Top). The length of the force profiles depends on the receptor conformation. In all simulations, considerably longer force profiles were observed for receptor conformation A. However, the initial receptor conformation does not correlate with the shape of the respective unbinding force profiles (Fig. S6B). Further, the rmsd of all backbone atoms of each HA head group were monitored during the receptor unbinding and compared to the unbinding forces (Fig. S6A). During receptor removal, the rmsd (Fig. S6A, Bottom) remained within their equilibrium fluctuations of 1.3 ± 0.2 Å (Fig. S6A, Bottom, gray area) and are not correlated to the unbinding forces (Fig. S6A, Top). As a consequence, the head groups of HA can be assumed to be at least structurally unaffected, and we regard the three parallel unbinding events per single simulations as independent from each other.

Next, we analyzed the receptor–HA interactions. The Coulombic and Lennard–Jones interaction energies (Fig. 4, Center and Bottom) show a strong correlation to the force profiles (Fig. 4, Top). At all force peaks—both from force profiles with single as well as with multiple peaks—a weakening of interaction energies was observed. Hence, force peaks can be linked to the rupture of receptor–HA interactions. In several cases we observed such weakening of interactions in the absence of a pronounced force peak (Fig. 4, blue stretches for receptors A and C), indicating spontaneous receptor release. Furthermore, we observed different changes in interaction energies at individual force peaks. In most cases, a weakening of both Coulombic and Lennard–Jones energy contributions occurred. However, in some cases a more pronounced weakening of Lennard–Jones interactions reveals

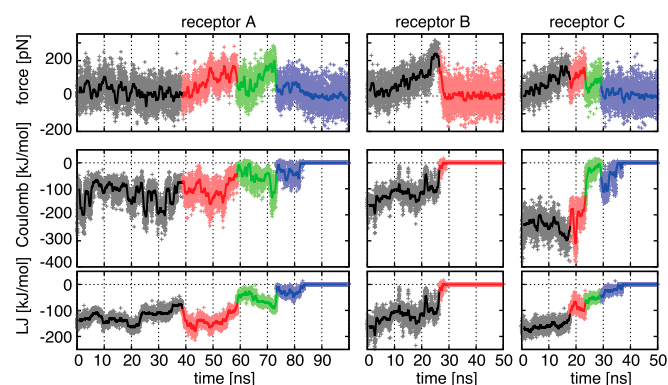


Fig. 4. Force and energy spectra for a particular simulation. Forces (Top) and protein–receptor interaction energies (Middle and Bottom) from unbinding events of all three receptors (single columns) of a representative simulation at pulling speed $v = 0.05$ m/s. Also shown are Coulombic (Middle) and Lennard–Jones (Bottom) interactions. Both raw data (symbols) and Gauss-filtered data (lines) are shown. The different colors are used to differentiate between distinct steps of the unbinding process. Columns labeled as receptors A–C refer to receptors A–C from Fig. S5.

a partial release of the receptor from the HA binding pocket (e.g., Fig. 4, receptor C, transition from black to red).

This diverse behavior both on a global scale (single and multiple force peaks) as well as on a local scale (energy contributions) strongly indicates the presence of different unbinding pathways. Snapshots at several stages of the simulations revealed a broad variety of atomic interactions that stabilize the receptors within the binding pocket. As an example, the release of a receptor in conformation C was analyzed in more detail (Fig. 5). In the initial phase, a set of six hydrogen bonds stabilizes the receptor (dashed, colored lines in Fig. 5I). Later, the receptor gets extended, but is still held back by hydrogen bonds originating from the binding pocket (Fig. 5II). During this phase, new hydrogen bonds are formed (e.g., Glu190, cyan) or existing ones get replaced by new ones (e.g., Asn137, blue). The rupture of hydrogen bonds (transitions from Fig. 5II to III and III to IV, respectively) is accompanied by a force peak (Fig. 5, Right). In this example, a sequential rupture of hydrogen bonds in the order of Ser136 together with Asn137 at 17.8 ns (Fig. 5II), Tyr98 together with Glu190 at 23.5 ns (Fig. 5III), and Gly135 at 29.3 ns (Fig. 5IV), leads to a force profile with multiple force peaks. Each rupture event of one or more hydrogen bonds causes a subpeak in the force profile. In contrast, the parallel rupture of all active hydrogen bonds causes a force profile with a single peak. In this scenario, either all initial hydrogen bonds are still intact or, contrarily, only a few hydrogen bonds are left after spontaneous rupture of the other hydrogen bonds without the occurrence of force peaks (e.g., Fig. 5, Thr187). Further, a reformation of hydrogen bonds after initial rupture as well as the transient formation of new hydrogen bonds were also observed (e.g., Ser136 and Asn137, approximately 18–20 ns), often causing additional force peaks. This way, many unbinding pathways are possible. These depend both on the initial receptor conformation and the corresponding interactions as well as on thermal fluctuations during the unbinding.

Comparison of Experiment and Simulation. Evidently, the loading rate applied by AFM and optical tweezers is much slower than that necessarily employed in the relatively short MD simulations. Nevertheless, to allow comparison of the measured forces with those calculated from the simulations, we used a scaling theory (Eq. 1) that predicts logarithmic loading rate (or velocity) dependence of rupture forces over a wide range of time scales (11):

$$F(kv_p) = \frac{\Delta G^\ddagger}{v x^\ddagger} \left\{ 1 - \left[\frac{1}{\Delta G^\ddagger} \ln \frac{k_0 \exp(\Delta G^\ddagger + \gamma)}{x^\ddagger kv_p} \right]^v \right\} + f_R kv_p, \quad [1]$$

where k is the spring constant of the optical tweezer and the pull potential, and v_p is the probe velocity. Otherwise, ΔG^\ddagger and x^\ddagger denote the height and location of the energy barrier, respectively; k_0 is the intrinsic rate coefficient; $\gamma = 0.577$ is the Euler–Mascheroni constant; and v describes the shape of the energy barrier (11). The last term accounts for friction effects at high probe velocities with a friction coefficient f_R .

The theory fits both experimental and calculated rupture forces reasonably well (Fig. 6), and from the fit one obtains $s\Delta G^\ddagger = 20.3 k_B T$, $x^\ddagger = 0.63$ nm, $k_0 = 1630$ s^{-1} , $v = 5.4 \cdot 10^{-5}$, and $f_R = 31.8$ s. Deviations are seen at both small experimental loading rates that do not match the logarithmic slope of the fit well, as well as, to a lesser extent, high loading rates. Furthermore, although a stability analysis showed that the four parameters obtained from the above fit are well-defined, the parameter v for the shape of the energy barrier turned out to be much smaller than expected for an energy landscape with a barrier with a typical shape (for which $v = 0.1 \dots 2$). Both observations suggest that different parts of the underlying free energy landscape govern unbinding at the two ends of the probed time scales. Although

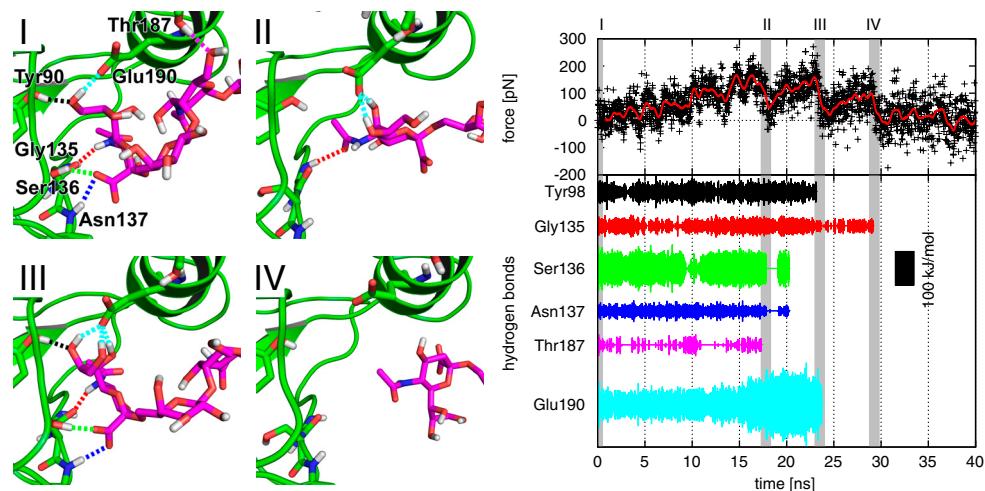


Fig. 5. Ligand unbinding event. (*I–IV*) Different snapshots of the receptor (magenta, sticks) being pulled toward the right side, away from HA (green, cartoon). Green sticks represent key residues from HA. Hydrogen bonds between key residues of HA and the ligand are shown as dashed lines. Snapshots were taken at 0, 17.8, 23.5, and 29.3 ns, respectively. (*Right*) Unbinding forces (*Top*) and strength of key hydrogen bonds (*Bottom*). Both unfiltered (black symbols) and Gauss-filtered (red line) forces are shown. Vertical gray bars depict the snapshot times of *I–IV*. Here, hydrogen bonds in *I–IV* are indicated by identical colors.

the obtained parameters may differ at slow and fast time scales, we assume that the above complexity, reflected by the heterogeneity of unbinding paths and forces for fast unbinding, also holds for slower unbinding.

Discussion

We used AFM and optical tweezers-based force spectroscopy to measure the interaction forces between single influenza viruses and living cells. Despite the possibility of trapping even single viruses (12), it is much more accurate to use a bigger sample carrier, which allows precise calibration of the optical trap. We coated PS beads by nonspecific adsorption, a common sample-probe attachment method in AFM and OT-based force spectroscopy experiments (13, 14). Here, the benefit of using spherical beads also involves limitations. The contact area between bead and cell surface is very large, which in the first place decreased the chance to detect single virus–receptor interactions. Hence, we used a low virus concentration on the bead. However, more specific and resistant attachment protocols have been developed (15) and, as a complementary method, we used an AFM-based approach. Here, influenza virions were covalently attached to

the AFM tip by using a bifunctional cross-linker. Both methods revealed unbinding forces between 7 and 25 pN. These forces are much lower than the adhesive forces between polystyrene and proteins (8), ensuring stable attachment of viruses on the bead surface during the force measurements. The reliability of our optical tweezers approach is confirmed by similar results with AFM, which was successfully used previously to measure cell adhesion forces of human rhinovirus (HRV) and HIV (10, 16).

Dynamic force spectroscopy, by varying the pulling velocity, revealed the characteristics of the underlying interaction. We observed a broad distribution of unbinding forces, which led to an increased uncertainty of the values for k_{off} and x_u . This correlates with a broad distribution of unbinding pathways and rupture forces in MD simulations. The obtained values describe a notably weak interaction compared to other lectin–carbohydrate bonds like concanavalin A (17) or *Helix pomatia* Lectin (18). Compared to surface plasmon resonance measurements (SPR) of the interaction between HA and fetuin (19), a highly glycosylated blood plasma protein, we observed dissociation rates that are about 10^3 times higher. Because high rebinding rates often interfere with SPR experiments, the detected dissociation rates can be drastically decreased. This is apparent in the case of multivalent interactions and shows the dynamic of this interaction type. Such differences between molecular and cellular dissociation were observed previously for HRV and HIV cell adhesion (10, 16) and underline the suitability of SVFS experiments to investigate binding between live cells and virions. For AFM, we used different cell lines and virus strains. The cells are characterized to contain predominately 2,3-(CHO cells) or a mixture of 2,3- and 2,6-linked sialic acids (MDCK and A549). However, for both virus strains we did not find a clear preference for one of the cell lines. Further, in MD simulations using 2,3-linked SA (LSTa), we found very similar force values compared to 2,6-linked SA in LSTc (Fig. S7), which agrees with the observations made during the AFM virus–cell pulling experiments. From NMR studies with purified ligands (20), the dissociation constant of X-31 HA to sialylactose was reported to be 2.1 mM (2,6 linked) and 3.2 mM (2,3 linked). We suppose that these rather small differences observed using purified binding partners may not become obvious under conditions mimicking more closely the biological situation, as in our study. Further, in a fluorescence-based binding assay we obtained similar results, indicating that both virus strains bind the probed cell line at equal amounts (Fig. S8). We surmise that this is an intrinsic property of the HA–SA interaction, perhaps related to the structure of the cellular receptors exposing SA.

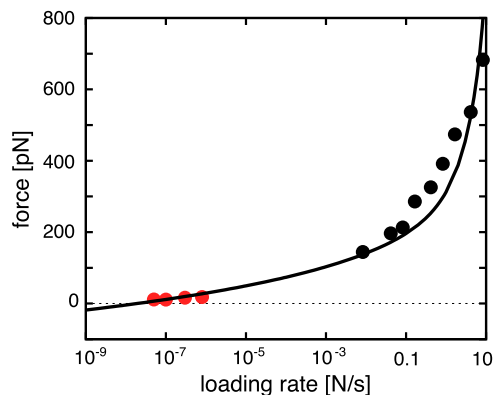


Fig. 6. Comparison of peak forces from optical tweezers and MD simulations. Data obtained from optical tweezers (red circles) and MD simulations (black circles) were fitted to Eq. 1 (black line). The MD datapoints represent the mean rupture force of all unbinding events at the indicated pulling velocity. The fitted curve describes the general dependence of rupture forces on the probe velocity but lacks matching detail at high and very low loading rates. This suggests a more complex energy, presumably with two energy barriers. The dotted line marks the zero-force level.

It was shown previously that the unique environment of the receptor within the plasma membrane strongly affects affinity for the virus (10).

MD simulations provide detailed information on the molecular structures and unbinding pathways that govern the interaction forces. In free simulations we observed that each receptor takes a slightly different conformation, although hydrogen bonds between four HA residues (Tyr98, Gly135, Ser136, and Asn137) and the receptor were always present, which is consistent with previous simulations (21, 22). These four amino acids belong to the base and loop 130 of the HA receptor-binding pocket and are highly important for binding to the receptor (1). Mutation of Tyr98 completely abolishes red blood cell binding, which highlights the importance of this hydrogen bond to the terminal SA of the receptor (23). The HA-receptor linkage is exclusively mediated by nonbonded interactions originating from Coulomb and Lennard–Jones interactions, which include Pauli repulsion as well as van der Waals attraction. Our analysis shows that these two regimes contribute almost equally to the unbinding force. Remarkably, the force simulations reveal a broad spectrum of unbinding pathways. The interaction appears very dynamic, including spontaneous release and rebinding of the receptor to HA. Zipper-like and all-or-none unbinding events were observed for all three receptors. These differences cannot be observed with experimental force spectroscopy, where single force peaks were detected during unbinding. It was shown previously that unbound LSTc in solution adopts multiple conformations, which are strongly reduced upon binding to HA (22). This intrinsic structural variability of the receptor is also present in our unbinding simulations. Rupture of individual bonds gives the ligand some flexibility, allowing rebinding and eventual unbinding.

The time scale of AFM and OT experiments is in the range of milliseconds to seconds and confronts nanoseconds in MD simulations. By using all three methods we observed that the measured unbinding force increased with faster extraction velocity. We used a theory that predicts a logarithmic velocity dependence to compare the rupture forces observed in the simulations with those measured by OT at much slower extraction velocities (11), and found reasonable, albeit imperfect, correlation between experiment and simulation. This observation suggests a more complex energy landscape of the underlying interaction, presumably with more than one barrier and pathway. This type of inter-

action was observed previously for HIV (24). However, the structural origin and shape of the second energy barrier remains to be elucidated by SVFS at higher loading rates.

Materials and Methods

SVFS Using Optical Tweezers. For OT measurements we used the JPK Instruments NanoTracker (25) with a 1,064-nm laser (3 W). For calibration of the optical trap, the Brownian motion of a bead at defined laser intensities was measured. The power spectrum of the diffusive motion exerted by a particle in a viscous liquid and held by a trap of stiffness k can be fitted to a Lorentzian curve. This provides the trap stiffness k and, together with the detector sensitivity, the signals can be calibrated either in nanometer displacement or piconewton forces. The value of impingement force, ranging between 10 to 50 pN, was selected to promote single-bond formation between virus and host cell receptors. All measurements were carried out in PBS buffer at 37 °C.

SVFS Using Atomic Force Spectroscopy. AFM-based force spectroscopy was performed with an Agilent 5500 AFM combined with an iMIC microscope (TILL Photonics). The Petri dish with cells was mounted with the AFM, which was put on the optical microscope through a specially designed XY stage. Before force measurements, the cantilever with a nominal spring constant of 10 pN/nm functionalized with influenza A X-31 was incubated in 5 mg/mL BSA for 30 min in order to minimize the nonspecific interaction between the cantilever tip and the cell surface. Measurements were performed in PBS buffer at RT. After the cantilever tip approached to the cell surface, force distance curves were repeatedly measured with Z-scanning range of 2 μm , cycle duration of 0.5–8 s, 500 datapoints per curve, and typical force limit of about 40–70 pN.

MD Simulations. All simulations were performed using GROMACS 4.0 (26, 27). The AMBER99SB force field (28) was used to describe protein atoms and ions; sugar molecules were described by the GLYCAM 06 force field (29). All simulations were carried out in explicit solvent, using the extended simple point charge (SPCE) water model (30). Lennard–Jones interactions were cut off beyond 1 nm. Coulomb interactions were calculated explicitly below 1 nm and by Ewald summation (31, 32) beyond that distance. The temperature was kept constant at 300 K using a Berendsen thermostat (33) with a coupling time of 0.1 ps. A Berendsen barostat (33) with a coupling time of 1 ps and a compressibility of $4.5 \cdot 10^{-9} \text{ bar}^{-1}$ was employed to maintain a pressure of 1 bar. All bond lengths were constrained using LINCS (34). An integration step of 2 fs and periodic boundary conditions were used (*SI Materials and Methods*).

ACKNOWLEDGMENTS. The project was supported by the Deutsche Forschungsgemeinschaft, SFB 765 TP C6 (to A.H.).

1. Skehel JJ, Wiley DC (2000) Receptor binding and membrane fusion in virus entry: The influenza hemagglutinin. *Annu Rev Biochem* 69:531–569.
2. Weis W, et al. (1988) Structure of the influenza virus haemagglutinin complexed with its receptor, sialic acid. *Nature* 333:426–431.
3. Couceiro JN, Paulson JC, Baum LG (1993) Influenza virus strains selectively recognize sialyloligosaccharides on human respiratory epithelium: The role of the host cell in selection of hemagglutinin receptor specificity. *Virus Res* 29:155–165.
4. Eisen MB, Sabesan S, Skehel JJ, Wiley DC (1997) Binding of the influenza A virus to cell-surface receptors: Structures of five hemagglutinin–sialyloligosaccharide complexes determined by X-ray crystallography. *Virology* 232:19–31.
5. Neuman KC, Nagy A (2008) Single-molecule force spectroscopy: Optical tweezers, magnetic tweezers and atomic force microscopy. *Nat Methods* 5:491–505.
6. Hinterdorfer P, Dufrène YF (2006) Detection and localization of single molecular recognition events using atomic force microscopy. *Nat Methods* 3:347–355.
7. Grubmüller H, Heymann B, Tavan P (1996) Ligand binding: Molecular mechanics calculation of the streptavidin–biotin rupture force. *Science* 271:997–999.
8. Sagvolden G, Gjaever I, Pettersen EO, Feder J (1999) Cell adhesion force microscopy. *Proc Natl Acad Sci USA* 96:471–476.
9. Evans E, Ritchie K (1997) Dynamic strength of molecular adhesion bonds. *Biophys J* 72:1541–1555.
10. Rankl C, et al. (2008) Multiple receptors involved in human rhinovirus attachment to live cells. *Proc Natl Acad Sci USA* 105:17778–17783.
11. Dudko OK, Hummer G, Szabo A (2006) Intrinsic rates and activation free energies from single-molecule pulling experiments. *Phys Rev Lett* 96:108101.
12. Ashkin A, Dziedzic JM (1987) Optical trapping and manipulation of viruses and bacteria. *Science* 235:1517–1520.
13. Rief M, Gautel M, Oesterhelt F, Fernandez JM, Gaub HE (1997) Reversible unfolding of individual titin immunoglobulin domains by AFM. *Science* 276:1109–1112.
14. Li C, Liu KK (2008) Nanomechanical characterization of red blood cells using optical tweezers. *J Mater Sci Mater Med* 19:1529–1535.
15. Ebner A, et al. (2009) *Handbook of Single-Molecule Biophysics*, eds P Hinterdorfer and A van Oijen (Springer, Heidelberg), pp 407–449.
16. Dobrowsky TM, Zhou Y, Sun SX, Siliciano RF, Wirtz D (2008) Monitoring early fusion dynamics of human immunodeficiency virus type 1 at single-molecule resolution. *J Virol* 82:7022–7033.
17. Chen A, Moy VT (2008) Cross-linking of cell surface receptors enhances cooperativity of molecular adhesion. *Biophys J* 78:2814–2820.
18. Grandbois M, Dettmann W, Benoit M, Gaub H (2000) Affinity imaging of red blood cells using an atomic force microscope. *J Histochem Cytochem* 48:719–724.
19. Takemoto DK, Skehel JJ, Wiley DC (1996) A surface plasmon resonance assay for the binding of influenza virus hemagglutinin to its sialic acid receptor. *Virology* 217:452–458.
20. Sauter NK, et al. (1992) Binding of influenza virus hemagglutinin to analogs of its cell-surface receptor, sialic acid: Analysis by proton nuclear magnetic resonance spectroscopy and x-ray crystallography. *Biochemistry* 31:9609–9621.
21. Newhouse EI, et al. (2009) Mechanism of glycan receptor recognition and specificity switch for avian, swine, and human adapted influenza virus hemagglutinins: A molecular dynamics perspective. *J Am Chem Soc* 131:17430–17442.
22. Xu D, et al. (2009) Distinct glycan topology for avian and human sialopentasaccharide receptor analogues upon binding different hemagglutinins: A molecular dynamics perspective. *J Mol Biol* 387:465–491.
23. Martin J, et al. (1998) Studies of the binding properties of influenza hemagglutinin receptor-site mutants. *Virology* 241:101–111.
24. Chang MI, Panorchan P, Dobrowsky TM, Tseng Y, Wirtz D (2005) Single-molecule analysis of human immunodeficiency virus type 1 gp120-receptor interactions in living cells. *J Virol* 79:14748–14755.
25. Wozniak A, van Mameren J, Ragona S (2009) Single-molecule force spectroscopy using the NanoTracker optical tweezers platform: From design to application. *Curr Pharm Biotechnol* 10:467–473.
26. Van Der Spoel D, et al. (2005) GROMACS: Fast, flexible, and free. *J Comput Chem* 26:1701–1718.

27. Hess B, Kutzner C, van der Spoel D, Lindahl E (2008) GROMACS 4: Algorithms for highly efficient, load-balanced, and scalable molecular simulation. *J Chem Theory Comput* 3:435–447.
28. Hornak V, et al. (2006) Comparison of multiple Amber force fields and development of improved protein backbone parameters. *Proteins* 65:712–725.
29. Kirschner KN, et al. (2008) GLYCAM06: A generalizable biomolecular force field. Carbohydrates. *J Comput Chem* 29:622–655.
30. Berendsen HJC, Postma JPM, van Gunsteren WF, Hermans J (1981) *Intermolecular Forces*, ed B Pullman (D. Reidel, Dordrecht), pp 331–342.
31. Darden T, York D, Pedersen L (1993) Particle mesh Ewald: An $N \cdot \log(N)$ method for Ewald sums in large systems. *J Chem Phys* 98:10089–10092.
32. Essmann U, et al. (1995) A smooth particle mesh Ewald method. *J Chem Phys* 103:8577–8592.
33. Berendsen H, Postma J, van Gunsteren A, Di Nola A, Haak J (1984) Molecular dynamics with coupling to an external bath. *J Chem Phys* 81:3684–3690.
34. Hess B, Bekker H, Berendsen H, Fraaije J (1997) LINCS: A linear constraint solver for molecular simulations. *J Comput Chem* 18:1463–1472.